IMAV2017-16
http://www.imavs.org/pdf/imav.2017.16

Incremental Nonlinear Dynamic Inversion and Multihole Pressure Probes for Disturbance Rejection Control of Fixed-wing Micro Air Vehicles

Elisabeth S. van der Sman,* Ewoud J. J. Smeur, Bart Remes, Christophe De Wagter, and Qiping Chu
Delft University of Technology, 2629 HS Delft, The Netherlands

ABSTRACT

Maintaining stable flight during high turbulence intensities is challenging for fixed-wing micro air vehicles (MAV). Two methods are proposed to improve the disturbance rejection performance of the MAV: incremental nonlinear dynamic inversion (INDI) control and phase-advanced pitch probes. INDI uses the angular acceleration measurements to counteract disturbances. Multihole pressure probes measure the incoming flow angle and velocity ahead of the wing in order to react to gusts before an inertial response has occurred. The performance of INDI is compared to a traditional proportional integral derivative (PID) controller with and without the multihole pressure probes. The attitude controllers are tested by performing autonomous wind tunnel flights and stability augmented outdoor flights. This paper shows that INDI improves the disturbance rejection performance of fixed-wing MAVs compared to traditional proportional integral derivative controllers.

1 INTRODUCTION

THE number of Micro Air Vehicles (MAVs) flying in urban areas is increasing due to the low cost, the low weight, the availability of ready-to-use platforms and the variety of applications. Fixed-wing MAVs are ideal for tasks which require a long range and endurance such as mapping the environment, surveillance, photography and delivering goods. These tasks may require the MAV to fly between buildings and obstacles which generate high energy turbulence [1]. The turbulence intensity profile increases as the MAV flies closer to the ground reaching levels up to 50% [2]. The perceived turbulence level depends on the MAV flight speed. The lower the flight speed the higher the turbulence intensity, indicating that hover is the most critical condition for MAVs [3]. Fixed-wing MAVs are particularly susceptible to wind gusts due to the large wing area [3]. Mohamed et al. identified two main approaches to counteract turbulence: reactive and phase-advanced [2]. Reactive techniques use sensors to measure the inertial response to disturbances. This paper focuses on developing a reactive nonlinear controller in combination with phase-advanced sensors to increase the stability of fixed-wing MAVs flying through turbulence.

Gusts cause large variations in airspeed and attitude angles in MAV, leading to nonlinear behavior. To maintain an optimal performance gain scheduling is needed [4]. Alternatively, using the model based Nonlinear Dynamic Inversion (NDI) a uniform performance over the flight envelope is guaranteed if the aerodynamic model is accurately known [5]. The major disadvantage of NDI is the sensitivity to model mismatch [6]. Determining an accurate aerodynamic model of the MAV is very expensive and time consuming. It has been very successful in programs like the Lockheed Marting X-35 [7][8] and the NASA X-36 tailless aircraft [9]. Incremental Nonlinear Dynamic Inversion (INDI) [10][11][6] has been proposed to highly reduce model sensitivity. It relies on angular acceleration, filtered from differentiated angular rate provided by the gyroscopes[12]. Smeur et al. [12] found that the same filter should be used on the actuators to provide time synchronization with the measured acceleration. The only model parameters required by the INDI attitude controller are the actuator dynamics and the control effectiveness [12]. INDI has been implemented on fixed-wing MAVs for the first time by Vlaar [13].

Phase-advanced sensors are used to measure turbulence before an inertial response has occurred [14][15]. The first phenomenon to occur is the change in flow pitch angle and velocity ahead of the wing. These variations cause an uneven lift distribution over the wings leading to structural stresses which can be measured by strain sensors [16]. Mohamed et al. [2] developed a pitch probe sensor inspired by the leading edge feathers of birds. This sensor measures the variations in the angle of attack and speed of the incoming flow. By measuring the incoming gust ahead of the wing a time advantage is created. The gust is related to the pressure distribution over the wing which in turn causes an angular acceleration measurement. The sensor was therefore placed at the point of highest correlation between the surface pressure variation and the measured angular acceleration [16]. The gust measurement is used as a feed-forward component to each aileron separately to locally counteract the gust on each wing [2]. This sensor enhances the controller performance by decreas-

*Msc. Student, Control and Simulation Department, Faculty of Aerospace Engineering

ing the range of the roll and pitch angle displacements [2].

Wind tunnel flights were performed by inserting static turbulence generating grids at the inlet of the test section. The distance from the grids in the direction of the flow determines the turbulence intensity level experienced by the MAV [17]. Outdoor tests are performed with natural turbulence. The length scale of indoor turbulence is in the order of 1 meter compared to 15 meters for outdoor flights [2]. The aim of this paper is to investigate the disturbance rejection performance of INDI applied to fixed-wing MAVs in high turbulence intensities and to compare the performance of the proposed system with a traditional PID controller. Finally research is performed on the incorporation of the pitch probe sensors in the INDI control structure. All systems are implemented on the Slick 360 Micro fixed-wing MAV with the Open-Source Paparazzi Autopilot system. The disturbance rejection performance is tested in the same turbulence intensity conditions which are typical for urban environments.

The structure of this paper is the following: Section 2 describes the MAV model, Section 3 is dedicated to the design of the INDI and PID controllers and Section 4 describes the pitch probe sensors. Section 5 presents the experimental setup. The results are presented in Section 6.

2 MAV Model

The sum of moments experienced during flight by the Slick 360 Micro fixed-wing MAV expressed in the body frame are described by Eq. 1 [6] [18].

$$\dot{\mathbf{\Omega}} = \mathbf{I}^{-1}(\mathbf{M} - \mathbf{\Omega} \times \mathbf{I}\mathbf{\Omega}) \tag{1}$$

The sum of moments around the body axes $\{X_B, Y_B, Z_B\}$ is given by $\mathbf{M}^T = \begin{bmatrix} M_x & M_y & M_z \end{bmatrix}$. The angular rates are denoted by $\mathbf{\Omega}^T = \begin{bmatrix} p & q & r \end{bmatrix}$. The moment of inertia matrix is defined by Eq. 2 assuming a plane of symmetry around the longitudinal and vertical axis $(X_B Z_B - plane)$.

$$\mathbf{I} = \begin{bmatrix} I_{xx} & 0 & -I_{xz} \\ 0 & I_{yy} & 0 \\ -I_{xz} & 0 & I_{zz} \end{bmatrix} \tag{2}$$

The resulting system of equations is given by Eq. 3 [18] [19].

$$\begin{aligned} M_x &= I_{xx}\dot{p} + (I_{zz} - I_{yy})qr - I_{xz}(\dot{r} + pq) \\ M_y &= I_{yy}\dot{q} + (I_{xx} - I_{zz})rp + I_{xz}(p^2 - r^2) \\ M_z &= I_{zz}\dot{r} + (I_{yy} - I_{xx})pq - I_{xz}(\dot{p} + rq) \end{aligned} \tag{3}$$

Expressed in terms of the angular accelerations Eq. 3 becomes Eq. 4 [19].

$$\begin{aligned} \dot{p} &= (c_1 r + c_2 p)q + c_3 M_x + c_4 M_z \\ \dot{q} &= c_5 pr - c_6(p^2 - r^2) + c_7 M_y \\ \dot{r} &= (c_8 p - c_2 r)q + c_4 M_x + c_9 M_z \end{aligned} \tag{4}$$

The definitions of the multiplication parameters c_1 up to c_9 with $\Gamma = I_{xx}I_{zz} - I_{xz}^2$ [19]:

$$\begin{aligned} &\Gamma c_1 = (I_{yy} - I_{zz})I_{zz} - I_{xz}^2 && \Gamma c_3 = I_{zz} \\ &\Gamma c_2 = (I_{xx} - I_{yy} + I_{zz})I_{xz} && \Gamma c_4 = I_{xz} \\ &c_5 = (I_{zz} - I_{xx})I_{yy}^{-1} && c_6 = I_{xz}I_{yy}^{-1} \\ &c_7 = I_{yy}^{-1} && c_8 = (I_{xx} - I_{yy})I_{xx} - {I_{xz}}^2 \\ &\Gamma c_9 = I_{xx} \end{aligned}$$

The moments can be spit into two components Eq. 5: a part depending on the aerodynamic state variables and a part influenced by the control surfaces of the vehicle.

$$\mathbf{M} = \mathbf{M_a} + \mathbf{M_c} \tag{5}$$

Substituting Eq. 5 into Eq. 3 leads to Eq. 6 around the roll axis.

$$\begin{aligned} \dot{p} = (c_1 r + c_2 p)q + c_3 M_{x_a}(u, v, w, p, q, r) + \\ c_3 M_{x_c}(V, \delta_a, \delta_e, \delta_r) + c_4 M_{z_a}(u, v, \dot{v}, w, p, q, r) + \\ c_4 M_{z_c}(V, \delta_a, \delta_e, \delta_r)) \end{aligned} \tag{6}$$

In the body frame the components of the free stream velocity V are defined as u, v, w. The control surface deflections are denoted by $\delta_a, \delta_e, \delta_r$ for the ailerons, elevator and rudder respectively. Around the pitch axis substituting Eq. 5 into Eq. 3 leads to Eq. 7.

$$\begin{aligned} \dot{q} = c_5 pr - c_6(p^2 - r^2) + c_7 M_{y_a}(u, v, w, \dot{w}, p, q, r) + \\ c_7 M_{y_c}(V, \delta_a, \delta_e, \delta_r, \delta_t) \end{aligned} \tag{7}$$

A second derivative term is incorporated for the vertical velocity component $\dot{w}$. The thrust of the propeller is defined as δ_t.

Euler angles are used to define the orientation of the body frame with respect to the earth frame [18]. The kinematic attitude equations Eq. 8 for a flat non-rotating earth are used to relate the angular rates to the Euler angles [18].

$$\begin{aligned} \dot{\phi} &= p + q\sin\phi\tan\theta + r\cos\phi\tan\theta \\ \dot{\theta} &= q\cos\phi - r\sin\phi \\ \dot{\psi} &= q\tfrac{\sin\phi}{\cos\theta} + r\tfrac{\cos\phi}{\cos\theta} \end{aligned} \tag{8}$$

3 Incremental Nonlinear Dynamic Inversion

The angular accelerations around the body axes defined by Eq. 4 can be written in an incremental form by applying a Taylor series expansion. The resulting equation is used by the controller to predict the angular acceleration one step ahead in time based on the current time point [12].

3.1 Roll axis

Three eigenmotions characterize the behavior of the MAV around the roll axis: the aperiodic roll, the dutch roll and the spiral. The fast aperiodic roll is used to model the angular acceleration based on aileron inputs. During this maneuver the MAV is flown at a constant speed V of 10m/s with $\Delta u = 0$. The yawing motion and rudder input are neglected: $\Delta v = 0 \quad \Delta\dot{v} = 0 \quad \Delta r = 0 \quad \Delta\delta_r = 0$. Due

to this assumption the yaw moment M_z can be omitted [18]. The asymmetric and symmetric motions are considered decoupled. The effects of the symmetric motions are neglected: $\Delta\delta_e = 0 \quad \Delta w = 0 \quad \Delta q = 0$. Applying a Taylor series expansion to Eq. 6 with the above mentioned assumptions leads to Eq. 9.

$$\dot{p} = \dot{p}_0 + \frac{\partial(c_3 M_{x_a})}{\partial p}\bigg|_{p=p_0}(p - p_0) + \frac{\partial(c_3 M_{x_c})}{\partial \delta_a}\bigg|_{\delta_a=\delta_{a0}}(\delta_a - \delta_{a0}) \tag{9}$$

The partial derivative of the aerodynamic moment $\frac{\partial(c_3 M_{x_a})}{\partial p}$ is defined as F_p. The partial derivative of the control moment $\frac{\partial(c_3 M_{x_c})}{\partial \delta_a}$ is defined as G_{δ_a}, simplifying Eq. 9 to Eq. 10.

$$\Delta\dot{p} = F_p \Delta p + G_{\delta_a} \Delta\delta_a \tag{10}$$

A least-square fitting method is used to determine F_p and G_{δ_a}. Data was collected by performing outdoor test flights. In total 90 seconds of flight test data are used, 80% for the training set and 20% for the test set. An airspeed controller was used to maintain the cruise speed at 10m/s. During the flight p and δ_a were logged. $\dot{p}$ can be calculated by differentiating the angular rate. The change in $\dot{p}$ is too noisy to be used directly for the fit, all signals are therefore filtered with the same second order low pass filter given by Eq. 11 with $w_n = 15.9$ Hz and $\zeta = 0.65$.

$$H(s) = \frac{\omega_n^2}{s^2 + 2\zeta\omega_n s + \omega_n^2} \tag{11}$$

The root mean square error of the test set and training set differ by 2% indicating the model is not over-fitted. The model parameters are $F_p = -16 \pm 1\ [1/s]$ and $G_{\delta_a} = 212 \pm 6\ [rad/(s^2 rad)]$. The INDI controller is based on the principle of time scale separation [12] [6] simplifying Eq. 10 to Eq. 12.

$$\Delta\dot{p} = G_{\delta_a} \Delta\delta_a \tag{12}$$

The angular acceleration prediction of the INDI controller with damping Eq. 10 and without damping Eq. 12 are compared and shown in Figure 1. The root mean square error of the model without damping is 0.4% higher than with damping.

3.2 Pitch axis

Around the pitch axis the short period motion is modeled during cruise at 10m/s, with $\Delta u = 0$ [18]. The thrust input is kept constant: $\Delta\delta_t = 0$. The asymmetric motions are neglected leading to $\Delta v = 0 \quad \Delta p = 0 \quad \Delta r = 0 \quad \Delta\delta_a = 0 \quad \Delta\delta_r = 0$. The second order derivative is neglected $\Delta\dot{w} = 0$. With these assumptions Eq. 7 is simplified

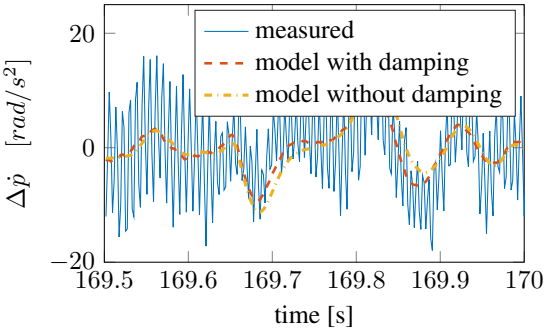

Figure 1: Measured and modeled angular acceleration: roll axis, $10m/s$

to Eq. 13.

$$\dot{q} = \dot{q}_0 + \frac{\partial(c_7 M_{y_a})}{\partial w}\bigg|_{w=w_0}(w - w_0) + \frac{\partial(c_7 M_{y_a})}{\partial q}\bigg|_{q=q_0}(q - q_0) + \frac{\partial(c_7 M_{y_c})}{\partial \delta_e}\bigg|_{\delta_e=\delta_{e0}}(\delta_e - \delta_{e0}) \tag{13}$$

The partial derivatives of the aerodynamic moment are defined as $F_q = \frac{\partial(c_7 M_{y_a})}{\partial q}$ and $F_w = \frac{\partial(c_7 M_{y_a})}{\partial w}$. The control effectiveness is defined as $G_{\delta_e} = \frac{\partial(c_7 M_{y_c})}{\partial \delta_e}$ leading to Eq. 14.

$$\Delta\dot{q} = F_w V \Delta\alpha + F_q \Delta q + G_{\delta_e} \Delta\delta_e \quad \alpha = w/V \tag{14}$$

To measure the angle of attack the MAV is placed in a pitch rig set-up where the MAV can only rotate around the pitch axis through the center of gravity. In this set-up the angle of attack α is considered equal to the pitch angle θ. A least-square fitting is used to determine F_w, F_q and G_{δ_e}. Open loop doublet inputs were applied in the wind tunnel at a speed of 10m/s. In total 45 seconds of flight test data are considered, 80% for the training set and 20% for the test set. During the flight q, θ and δ_e are logged. $\dot{q}$ is obtained by differentiating the angular rate. To decrease the noise level, all signals are filtered with the same second order low pass filter given by Eq. 11 with $w_n = 15.9$ Hz and $\zeta = 0.65$. The root mean square error of the test set and training set differ by only 0.2%. The model parameters are $F_w = -31.7 \pm 0.3\ [\frac{rad}{ms}]$, $F_q = -8.3 \pm 0.2\ [1/s]$ and $G_{\delta_e} = 73 \pm 1\ [rad/(s^2 rad)]$. The damping term F_w and the control effectiveness G_{δ_e} are in the same order of magnitude. This indicates the principle of time scale separation is theoretically no longer valid [6]. It is however, difficult to predict the value of the term $\Delta\alpha$ for the next time point. The INDI controller is therefore designed based on Eq. 15 considering errors can be present due to the effect of the damping term F_w.

$$\Delta\dot{q} = G_{\delta_e} \Delta\delta_e \tag{15}$$

The root mean square error of the model without damping is 22% higher compared to the model with damping. The increase in root mean square error is mainly due to the open loop response which includes a slow damping motion which is not captured by the initial elevator input. The damping is slower compared to the initial change in acceleration due to the elevator input and can therefore be compensated by a closed loop control structure. The comparison of the two models and the measured change in angular acceleration is given in Figure 2.

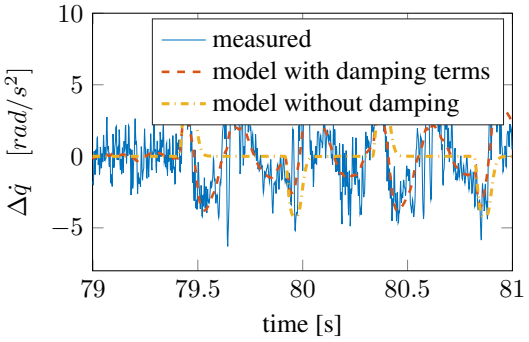

Figure 2: Measured and modeled angular acceleration: pitch axis, $10m/s$

3.3 Implementation

The INDI control scheme has the form given in Figure 3 and Figure 4 based on Eq. 12 and Eq. 15. The virtual control input v denotes the reference acceleration of the system which is compared to the measured acceleration $\dot{p}_f$ for roll and $\dot{q}_f$ for pitch. The subscript f is used to denote all signals which have been filtered with second order low pass filter $H(s)$. The inverse of the control effectiveness G is used to calculate the required change in input based on the angular acceleration error. This change in input cannot be achieved instantaneously but is filtered by the actuator dynamics $A(s)$. The actuator position that is achieved after a time step is fed back into the system delayed by the same filter $H(s)$ to achieve time synchronization with the angular acceleration. The linear PD controller is used to control the attitude angles. The controller uses the angular rate to calculate the derivative term. For small pitch angles this assumption is valid as shown by Eq. 8.

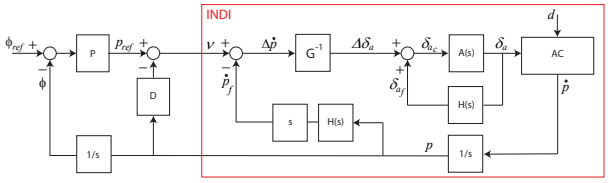

Figure 3: INDI control block structure roll

The actuators determine the reference tracking and disturbance rejection performance of the INDI controller [12].

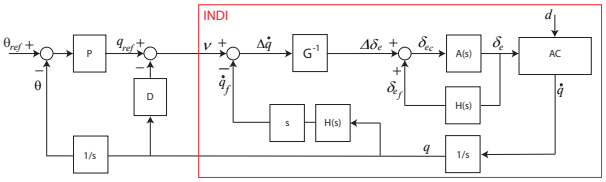

Figure 4: INDI control block structure pitch

The Slick 360 Micro uses 4 HK5330 micro servos to move the control surfaces. These servos are the fastest in this category currently available with a speed of 0.04 sec from 0 to 60 deg. The servo model is determined by logging the PWM command given by the autopilot and the position of the servo arm measured by the servo potentiometer. The servo is modeled as a first order system with a limited rate Eq. 16 and an initial delay of 10 milliseconds.

$$\begin{aligned} A(s) &= \tfrac{60}{s+60} \\ \left(\tfrac{\Delta\delta_a}{\Delta t} G_{\delta_a}\right)_{max} &= 11 \quad [rad/s] \\ \left(\tfrac{\Delta\delta_e}{\Delta t} G_{\delta_e}\right)_{max} &= 4 \quad [rad/s] \end{aligned} \tag{16}$$

3.4 Closed-loop Analysis

The closed-loop performance of the system can be calculated by simplifying the INDI controller to the actuator dynamics block shown in Figure 5 [12]. The actuator dynamics block contains a first order system and a rate limiter which is influenced by the control effectiveness G. Due to the rate limiter, increasing the PD gains does not necessarily lead to a faster reference tracking performance. During high turbulence intensities the system is considered to be operating in the range influenced by the rate limiter. The closed-loop response is analyzed for a step input of 0.2 rad for pitch and 0.4 rad for roll. Figure 6 shows the performance of the model with the parameters from Eq. 16 for $P = 100, 185, 300$ and 400. The ratio between the proportional and derivative gain should remain constant leading to a corresponding set of derivative gains $D = 12, 22, 36$ and 48. This shows that a drawback of using a higher P gain is the amplification of the noise in the roll and pitch rate signals due to a higher D gain. Figure 6 shows that the response of the system for a range of proportional gains is identical except for the last part of the step response where the first order system determines the behavior.

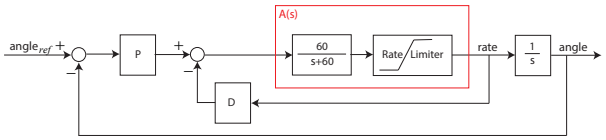

Figure 5: Linear gains analysis

Around the roll axis, the linear gains are designed to obtain a rise time of 0.22 sec given a step input of 0.4 rad without overshoot. This leads to $P = 185$ and $D = 22$. For pitch,

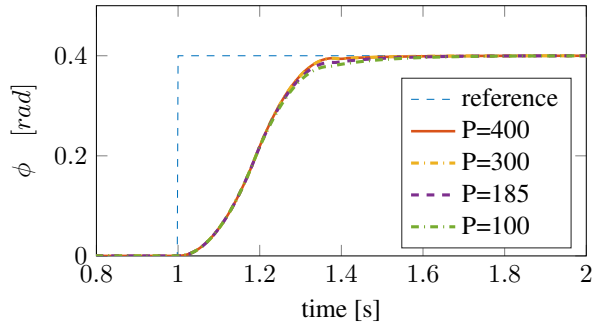

(a) Roll angle tracking of a step input of 0.4 radians

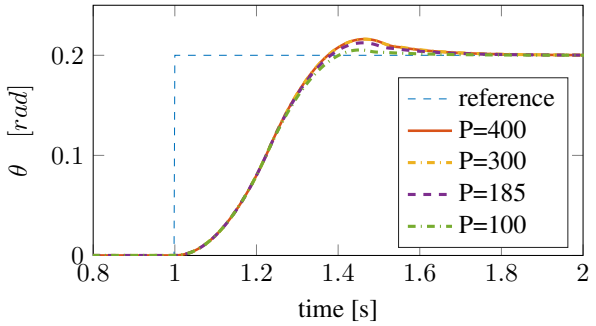

(b) Pitch angle tracking of a step input of 0.2 radians

Figure 6: Reference tracking performance for varying PD gains

the reference tracking for a step input of 0.2 rad is designed to give a rise time of 0.23 sec and a small overshoot of 6%. This leads to the same set of gains $P = 185$ and $D = 22$.

The PID gains used in this paper were manually tuned to obtain comparable rise time and overshoot properties as the INDI controller. For roll, the manually tuned P gain is 1.6 times higher compared to the INDI gain. The D gain used in the PID structure is 0.7 times lower compared to the INDI gain.

4 Phased-advanced pitch probes

The pressure probes system designed by Mohamed et al. [2] is used in the same configuration. The probe head is connected to a differential pressure sensor through acrylic tubes embedded in the wings. The probe is placed 15 cm ahead of the wing to create a 15 milliseconds time advantage at cruise speeds. The signals are feed-forwarded to both ailerons separately as shown in Figure 7 [2]. The probes sense changes in angle of attack of the incoming flow. Mohamed et al. [2] showed that a linear relationship between the angle of attack measurement and the differential pressure measurement. The probes are high pass filter using a fourth order Butterworth filter given by Eq. 17. Based on flight test data, the cut-off frequency was selected at 4Hz.

$$H(z) = \frac{b(1)+b(2)z^{-1}+b(3)z^{-2}+b(4)z^{-3}+b(5)z^{-4}}{a(1)+a(2)z^{-1}+a(3)z^{-2}+a(4)z^{-3}+a(5)z^{-4}} \quad (17)$$

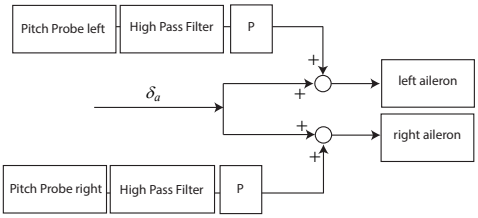

Figure 7: Feed-forward control probes [2]

with $b = \begin{bmatrix} 0.7194 & -2.8774 & 4.3162 & -2.8774 & 0.7194 \end{bmatrix}$ and $a = \begin{bmatrix} 1 & -3.3441 & 4.2389 & -2.4093 & 0.5175 \end{bmatrix}$.

5 Experimental set-up

Figure 8: Slick 360 Micro

The tests presented in this paper are all performed with the Slick 360 Micro shown in Figure 8. The MAV weighs 130 grams and has a wing span of 49 cm. The MAV is equipped with the LISA M Paparazzi open-source autopilot system and the phase-advanced pitch probes developed by Mohamed et al. [2]. Tests were performed in the Open Jet Facility (OJF) at Delft University of Technology and outdoors during a windy day. To ensure the human element is not influencing the results the MAV is flown completely autonomously with a vertical, longitudinal and lateral position control system.

5.1 Open Jet Facility

The OJF tunnel cross section is 285×285 cm. In the wind tunnel the coordinate system is defined as: X_w to the right perpendicular to the flow direction, Y_w in the direction of the tunnel flow and Z_w to the top of the wind tunnel. The origin of the axis system is given in Figure 9 in the middle of the cross section underneath the tunnel inlet. The head-

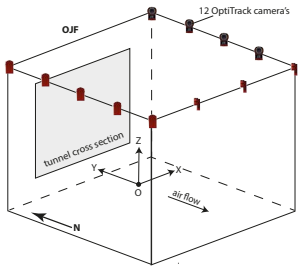

Figure 9: OJF wind tunnel coordinate system definition

ing is defined as $0\,\mathrm{deg}$ in the flow direction. The position is measured by 12 Optitrack cameras and sent at 20Hz.

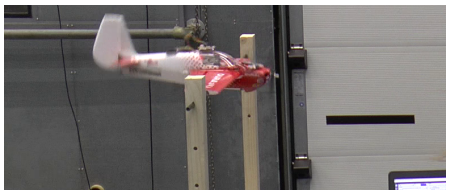

Figure 10: Pitch rig set-up

The pitch rig wind tunnel tests were performed to analyze the short period motion. The rig consists of a wooden construction attached to the tunnel floor and a movable rod connected to the wooden frame through low friction bearings. The rotational axis of the rig passed through the quarter chord line which corresponds to the center of gravity of the MAV. The pitch rig set-up is shown in Figure 10.

To replicate high levels of turbulence intensity static grids were placed at the test section inlet. The grids are built up of metal rods evenly spaced in the vertical direction and connected at the edges as shown in Figure 11. Close to the grids wake turbulence is generated which slowly decays into homogeneous turbulence [17]. This decay is captured by the variation of the turbulence intensity in the flow direction. The results shown in Section 6 are therefore always compared at the same $\{X_w, Y_w, Z_w\}$ position.

Figure 11: Turbulence grids set-up

5.2 Position Control

The MAV has to fly in a box with a maximum cross section of 285×285 cm minus the wing span. The position in the flow direction has to be constant to ensure the same level of turbulence intensity is experienced throughout multiple flights. In the wind tunnel the course angle cannot be used as the position of the MAV is constant and the MAV is effectively hovering. A heading based controller is used instead to control the lateral position.

5.2.1 Vertical and longitudinal control

The throttle is used to control the longitudinal displacements. During outdoor flights the throttle is only used for the climb and descent phases and therefore always combined with a corresponding pitch angle. The vertical controller uses the altitude error to calculate the reference climb rate. The altitude error is the difference between the reference altitude defined in the flight plan and the altitude z measured by the OptiTrack system. Based on climb rate, a feed-forward increase in throttle level on top of the cruise throttle is commanded. The longitudinal position y is compared to the reference position. A standard PID control structure is used to keep the aircraft at one location in the tunnel, as shown in Figure 12.

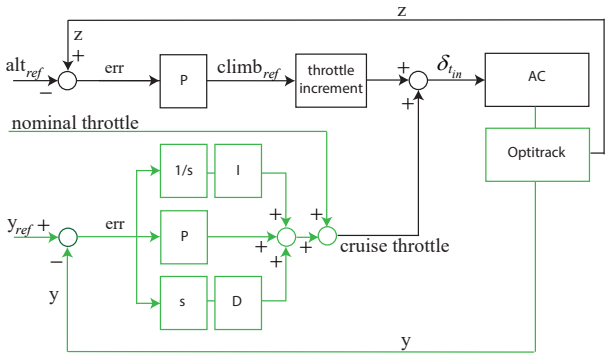

Figure 12: Vertical and longitudinal throttle control

The reference pitch angle is calculated from the desired climb rate which, as shown in Figure 13, depends on the altitude error.

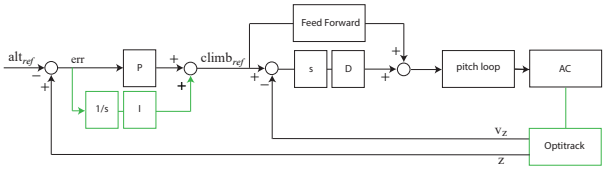

Figure 13: Vertical pitch control

5.2.2 Lateral control

The lateral controller defines a reference course (heading) angle χ_{ref} as the arctangent of the x and y distances between the MAV and the desired waypoint. A PD controller calculates the roll angle setpoint based on the heading error. An overview of the lateral position control block is given in Figure 14.

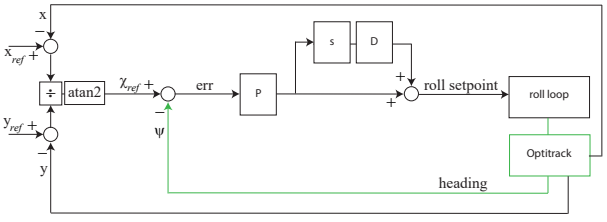

Figure 14: Lateral roll control

5.3 Outdoor test flights

The flight tests were performed in a field surrounded by trees to ensure the MAV is constantly subject to turbulence. The speed of the MAV was kept constant at 10m/s by a proportional integral (PI) airspeed controller regulating the throttle. The attitude was controlled by the test pilot. The turbulence length scale can be estimated by using the von Karman model given by Eq. 18 [17].

$$S_{\bar{u}\bar{u}}(f) = \frac{4\sigma^2 L_x}{V} \frac{1}{\left(1 + 70.8\left(\frac{L_x f}{V}\right)^2\right)^{\frac{5}{6}}} \tag{18}$$

$S_{\bar{u}\bar{u}}$ is the power spectral density as a function of the frequency f expressed in Hz. The power spectral density follows a -5/6 decay law as can be seen by the denominator of the function. σ is the standard deviation of the flow and L_x the turbulence length scale.

6 RESULTS

Table 1: Preliminary and final parameters of the INDI controllers

	Roll		Pitch	
	Preliminary	Final	Preliminary	Final
P	400	185	400	185
D	22	22	22	22
G	0.019	0.022	0.014	0.008
ω_n	3.2	15.9	1.6	15.9

Table 2: Preliminary and final parameters of the PID controllers

	Roll		Pitch	
	Preliminary	Final	Preliminary	Final
P	12500	15000	4500	16000
I	1	30	1	30
D	700	700	1.5	1.5

6.1 Wind Tunnel Flights

Approximate values of the control effectiveness, linear gains and filter cut-off frequency were used during the initial OJF windtunnel tests. The parameters calculated in Section 3 are summarized in Table 1 and Table 2 and compared to the empirically determined preliminary parameters used during the autonomous wind tunnel tests.

The INDI controller proved to be very precise and able to maintain the position within a 1x1x1 meter box during all flights. The performance of INDI and PID is evaluated for the same time frame and for the the same position $\{X_w, Y_w, Z_w\}$ and is shown in Figure 17.

The results given in Figure 15 and Figure 16 show that the range of the probability density function for the roll angle error decreases by 40% with the INDI controller compared to the PID controller. For the pitch angle the range

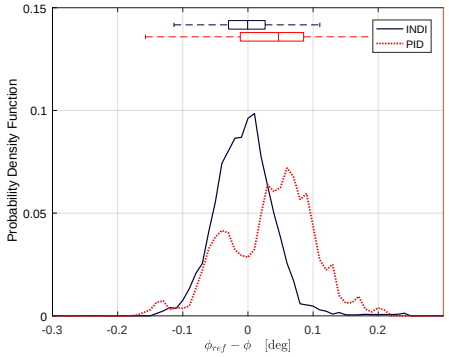

Figure 15: Roll angle perturbation for PID and INDI controller

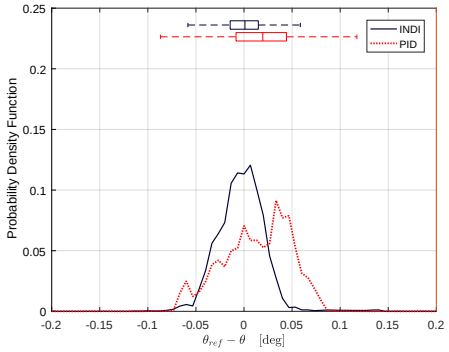

Figure 16: Pitch angle perturbation for PID and INDI controller

decreases by 43% for INDI compared to PID. The probability density functions of the PID controller for roll and pitch are not centered around zero. This indicates that the integral gains should be increased to obtain a better performance. The integral gains were therefore increased by a factor 30 for the final test flights, as shown in Table 2.

6.2 Outdoor flights

The reference tracking performance of the INDI controller around the roll axis is shown in Figure 18(a). The rise time of the step input given from 0 to 0.4 radians is on average 0.15 sec which is faster than the expected rise time obtained with the closed loop analysis in subsection 3.4 of Section 3. Overshoot is an average value of 10%. The reference tracking performance of the PID controller around the roll axis is shown in Figure 18(b) with an average rise time of 0.19 sec and overshoot of 5%. These tests were performed consecutively outdoors on the same day.

The reference tracking performance of the INDI controller around the pitch axis is shown in Figure 19(a). The rise time for the test performed at 10.6 m/s is 0.37 sec and the overshoot 13%. The variation between the three curves is due to the high levels of turbulence experienced during the flight and the different airspeeds at which the step inputs were given. The PID step response test was executed twice during this flight. The performance is difficult to assess due to the

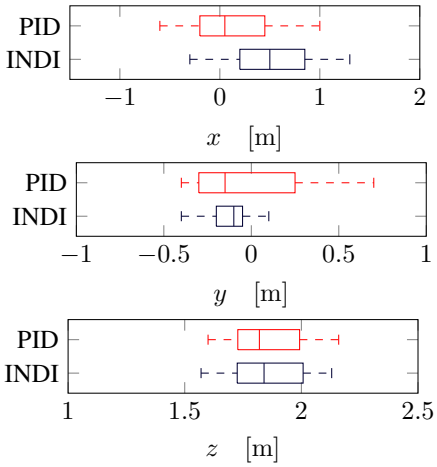

Figure 17: Position variation comparison between INDI and PID

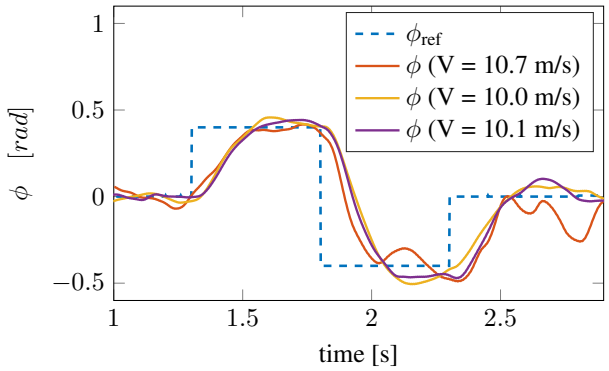

(a) INDI

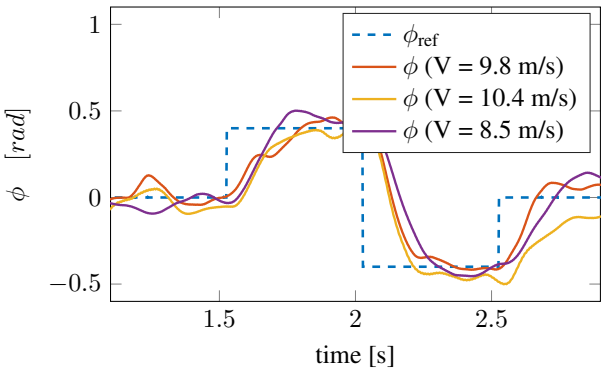

(b) PID

Figure 18: Roll axis tracking performance.

influence of high energy turbulence as shown in Figure 19(b). On a calm day the results obtained with the same PID gains show a very high performance as given in Figure 20. A small steady state-error is visible in the results indicating the tuning of the integral gain can be improved to eliminate the steady-state offset.

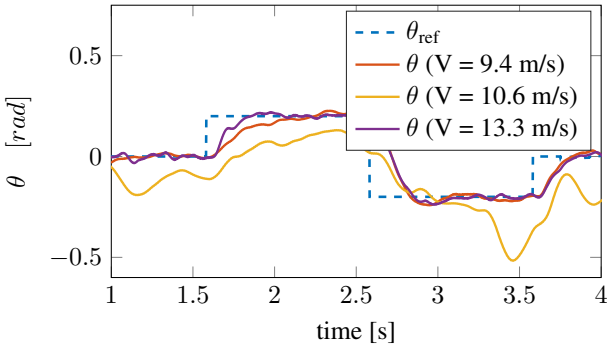

(a) INDI

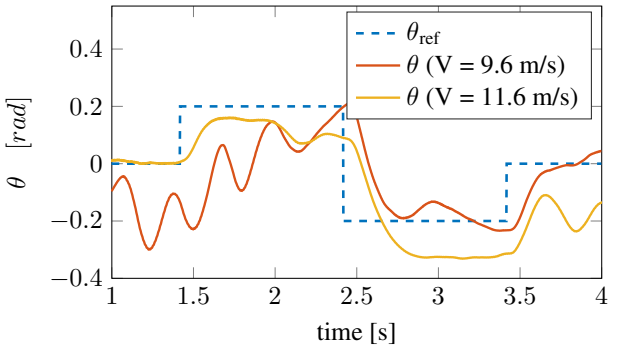

(b) PID

Figure 19: Pitch axis tracking performance.

The disturbance rejection of the INDI controller and the PID controller with and without pitch probes was tested on the same day while flying the same trajectory multiple times. The analysis of all test flights showed that one on the pitch probes got obstructed during landing causing a bias in the measurements of the subsequent flights. Therefore no reliable data was obtained on the performance of the INDI controller in combination with the pitch probe sensors. The disturbance rejection performance is therefore analyzed for the other three control approaches. In total 120sec of reliable flight data are analyzed in this section, 40 seconds for each controller. The turbulence intensity level of the flight data is $T_i = 12.9\%$. The turbulence length scale is estimated by using the von Karman spectrum Eq. 18 to be 2.5 meters. The performance is evaluated for the part of the flight which used the airspeed controller to maintain the average velocity around 10m/s. The average velocity of the flight test data is 9.7 m/s.

Figure 21(a) clearly shows an improvement in the probability density function of the roll angle error for the INDI

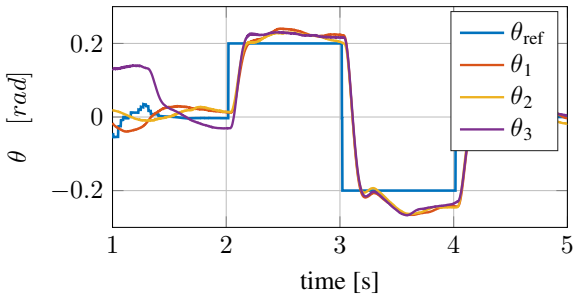

Figure 20: Pitch angle during doublet (PID, calm air, $10m/s$)

controller compared to the PID controller. The box plot of the data given in Figure 21(b) shows that the range decreases by 21% for INDI compared to PID. The enhanced PID controller with the pitch probes does not show an improvement in performance compared to the traditional PID controller. This result is not as expected from literature. Two main reasons have been identified which can influence the results: the high pass filter and degraded servos. The flight data show that the filtered probe values contain offsets. These offsets should have been eliminated by the high pass filter. The parameters used for the high pass filter during testing had a precision of 10^{-4}. By increasing the accuracy of the filter parameters to 10^{-6} all offsets are removed from the data. Another factor which was not taken into account is the degrading performance of the servos due to overheating. To eliminate this aspect the servos should be replaced after each test flight. Additional flight tests should be performed with accurate filter parameters and new servos to improve the performance of the pitch probe sensors.

The pitch angle error shown in Figure 22(a) also shows a clear improvement with INDI compared to PID. The box plot highlights the difference in Figure 22(b) which indicates that the range decreases by 24% for INDI compared to PID.

7 Conclusion

This research shows the potential of incremental nonlinear dynamic inversion applied to fixed-wing micro air vehicles flown in high turbulence intensities. The angular acceleration measurements are predicted based upon the control surface deflections eliminating the need for a complex aerodynamic model. To test the performance of the system a novel control solution is presented which allows autonomous free flight in a wind tunnel. The throttle is used for both the longitudinal an vertical control and the heading angle is used for lateral control. This experimental set-up eliminates all human factors and provides the opportunity to test in turbulence intensities which are beyond human capabilities. Autonomous free flight wind tunnel tests in turbulence were performed with estimates of the control effectiveness and the filter cut-off frequency. The performance of the estimated model is presented as it illustrates the robustness of the system. The

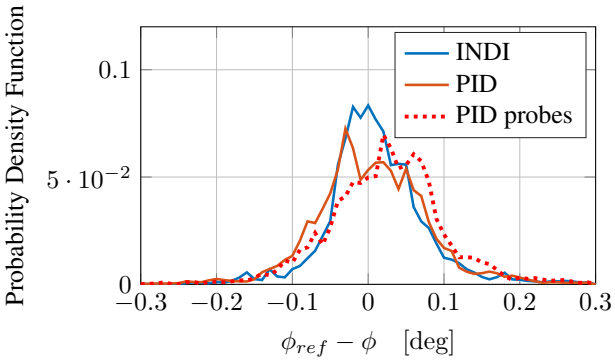

(a) Probability density function of the roll angle error

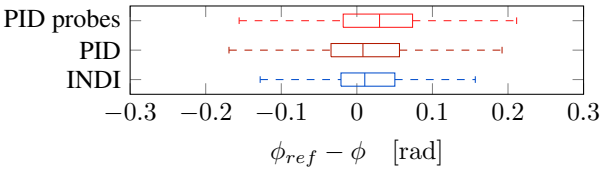

(b) Box plot of the roll angle error

Figure 21: Disturbance rejection performance around the roll axis

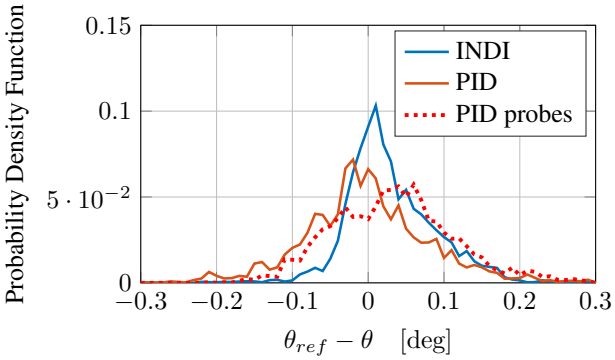

(a) Probability density function of the pitch angle error

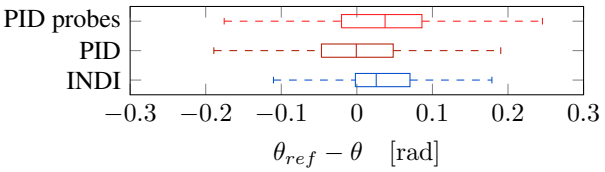

(b) Box plot of the pitch angle error

Figure 22: Disturbance rejection performance around the pitch axis

results show that the controller eliminates all steady-state errors and counteracts accelerations caused by external disturbances making it a suitable solution for precise movements in the wind tunnel. Accurate model parameters for the control effectiveness, the actuators and the filter cut-off frequency are determined in this paper and used to assess the performance of the system during outdoor test flights. During outdoor flights the performance is compared to a proportional integral derivative controller tuned to obtain the same reference tracking performance. The nonlinear incremental controller significantly improves the disturbance rejection performance around both the roll and pitch axis. More research should be performed to assess the performance of the nonlinear controller compared to an enhanced linear controller with phase-advanced pitch probes.

REFERENCES

[1] S. Watkins, A. Mohamed, A. Fisher, R. Clothier, R. Carrese, and D. F. Fletcher. Towards autonomous mav soaring in cities: Cfd simulation, efd measurement and flight trials. *International Micro Air Vehicles Conference and Flight Competition 2015*, 2015.

[2] A. Mohamed, M. Abdulrahim, S. Watkins, and R. Clothier. Development and flight testing of a turbulence mitigation system for micro air vehicles. *Journal of Field Robotics*, 33(5):639–660, 2016.

[3] S. Watkins, J. Millbank, B. J. Loxton, and W. H. Melbourne. Atmospheric winds and their implications for microair vehicles. *AIAA Journal*, 44(11):2591–2600, 2006.

[4] J. J. E. Slotine and W. Li. *Applied Nonlinear Control*. Prentice-Hall, 1991.

[5] H. P. Lee, S. E. Reiman, C. H. Dillon, and H. Youssef. Robust nonlinear dynamic inversion control for a hypersonic cruise vehicle. *AIAA Guidance, Navigation, and Control Conference and Exhibit*, 2007.

[6] S. Sieberling, Q. Chu, and A. J. Mulder. Robust flight control using incremental nonlinear dynamic inversion and angular acceleration prediction. *AIAA Journal of Guidance, Control, and Dynamics*, 33(6):1732–1742, 2010.

[7] K. Bordignon and J. Bessolo. Control allocation for the x-35b. *2002 Biennial International Powered Lift Conference and Exhibit*, 2002.

[8] G. P. Walker and D. A. Allen. X-35b stovl flight control law design and flying qualities. *2002 Biennial International Powered Lift Conference and Exhibit*, 2002.

[9] J. S. Brinker and K. A. Wise. Flight testing of reconfigurable control law on the x-36 tailless aircraft. *AIAA Journal of Guidance, Control, and Dynamics*, 24(5):903–909, 2001.

[10] P. R. Smith. A simpified approach to nonlinear dynamic inversion based flight control. *AIAA Atmospheric Flight Mechanics Conference and Exhibit*, 1998.

[11] B. J. Bacon and A. J. Ostroff. Reconfigurable flight control using nonlinear dynamic inversion with a special accelerometer implementation. *AIAA Guidance, Navigation, and Control Conference and Exhibit*, 2000.

[12] E. J. J. Smeur, Q. Chu, and G. C. H. E. de Croon. Adaptive incremental nonlinear dynamic inversion for attitude control of micro aerial vehicles. *AIAA Journal of Guidance, Control, and Dynamics*, 39(3):450–461, 2016.

[13] M. C. Vlaar. Incremental nonlinear dynamic inversion flight control implementation and flight test on a fixed wing uav. Master thesis, Delft University of Technology, Delft The Netherlands, February 2014.

[14] A Mohamed, R Clothier, S Watkins, R Sabatini, and M Abdulrahim. Fixed-wing mav attitude stability in atmospheric turbulence, part 1: Suitability of conventional sensors. *Progress in Aerospace Sciences*, 70:69–82, 2014.

[15] A Mohamed, S Watkins, R Clothier, M Abdulrahim, K Massey, and R Sabatini. Fixed-wing mav attitude stability in atmospheric turbulencepart 2: Investigating biologically-inspired sensors. *Progress in Aerospace Sciences*, 71:1–13, 2014.

[16] A. Mohamed, S. Watkins, R. Clothier, and M. Abdulrahim. Influence of turbulence on mav roll perturbations. *International Journal of Micro Air Vehicles*, 6(3):175–190, 2014.

[17] Sridhar Ravi. *The influence of turbulence on a flat plate aerofoil at Reynolds numbers relevant to MAVs*. PhD thesis, RMIT, Melbourne, Victoria, Australia, 2011.

[18] M. V. Cook. *Flight Dynamics Principles*. Elsevier, 2007.

[19] Lars Sonneveldt. *Adaptive Backstepping Flight Control for Modern Flighter Aircraft*. PhD thesis, Delft University of Technology, Delft, The Netherlands, 2010.